# The Stellar Distribution in Ultrafaint Dwarf Galaxies Suggests Deviations from the Collisionless Cold Dark Matter Paradigm

Jorge Sánchez Almeida[1,2] , Ignacio Trujillo[1,2] , and Angel R. Plastino[3]

[1] Instituto de Astrofísica de Canarias, La Laguna, Tenerife, E-38200, Spain; jos@iac.es

[2] Departamento de Astrofísica, Universidad de La Laguna, Spain

[3] CeBio y Departamento de Ciencias Básicas, Universidad Nacional del Noroeste de la Prov. de Buenos Aires, UNNOBA, CONICET, Roque Saenz Peña 456, Junin, Argentina

Abstract

Unraveling the nature of dark matter (DM) stands as a primary objective in modern physics. Here we present evidence suggesting deviations from the collisionless cold DM (CDM) paradigm. It arises from the radial distribution of stars in six ultrafaint dwarf (UFD) galaxies measured with the Hubble Space Telescope. After a trivial renormalization in size and central density, the six UFDs show the same stellar distribution, which happens to have a central plateau or core. Assuming spherical symmetry and isotropic velocities, the Eddington inversion method proves the observed distribution to be inconsistent with the characteristic potentials of CDM particles. Under such assumptions, the observed innermost slope of the stellar profile discards the UFDs to reside in a CDM potential at a $\geqslant 97\%$ confidence level. The extremely low stellar mass of these galaxies, 10^3–$10^4 \, M_\odot$, prevents stellar feedback from modifying the shape of a CDM potential. Other conceivable explanations for the observed cores, like deviations from spherical symmetry and isotropy, tidal forces, and the exact form of the used CDM potential, are disfavored by simulations and/or observations. Thus, the evidence suggests that collisions among DM particles or other alternatives to CDM are likely shaping these galaxies. Many of these alternatives produce cored gravitational potentials, shown here to be consistent with the observed stellar distribution.

Unified Astronomy Thesaurus concepts: Cold dark matter (265); Dark matter (353); Dark matter distribution (356); Dwarf galaxies (416); Star counts (1568)

1. Introduction

The shape of the dark matter (DM) haloes of low-enough mass galaxies encodes direct information on the nature of DM. Self-gravitating collisionless cold DM (CDM) halos evolving in a cosmological context develop a central cusp where the mass density profile increases toward the center following the Navarro–Frenk–White (NFW) profile or other similar shape (after Navarro et al. 1997; see also Wang et al. 2020). When baryons are included, baryonic processes can thermalize the overall gravitational potential turning the central cusp into a plateau or core (e.g., Governato et al. 2010), a mechanism invoked to explain the DM haloes observed in dwarf galaxies (e.g., Oh et al. 2015). The energy needed to turn cusps into cores must be extracted from the star formation; therefore, when the formed stellar mass is too small, the baryon feedback is unable to transform cusps into cores and the DM haloes remain cuspy. The actual largest stellar mass ($M_\star$) unable to modify the CDM potential is model dependent (Read et al. 2016) but it roughly corresponds to $M_\star < 10^6 \, M_\odot$ or to a DM halo mass $< 10^{10} \, M_\odot$ (Di Cintio et al. 2014; Chan et al. 2015; Hayashi et al. 2020; Jackson et al. 2021). Thus, if the DM haloes of these halo unevolved galaxies (HUGs) happen to show a core, it would indicate the DM not being collisionless, reflecting the much sought-after presently unknown true nature of the DM (fuzzy, self-interacting, warm, or other alternatives; e.g., Bechtol et al. 2022).

In practice, DM halo shapes are deduced from spatially resolved kinematical measurements, which require time-consuming high spectral resolution spectroscopy and are virtually impossible in the required HUG regime. Sánchez Almeida et al. (2023) proposed an alternative based on photometry, much cheaper observationally, but starting from a series of simplifying assumptions that must be justified a posteriori. It uses the classical Eddington inversion method (EIM; e.g., Binney & Tremaine 2008; Ciotti 2021), which provides the distribution function (DF) to be followed by a mass density profile immerse in a spherically symmetric gravitational potential. If the required DF becomes negative somewhere in the phase space, it proves the pair density–potential to be physically inconsistent with each other. Such inconsistency happens for a combination particularly interesting in the present context, namely, a stellar density with a core residing in an NFW potential (An & Evans 2006, 2009; Sánchez Almeida et al. 2023). Stellar cores seem to be quite common in low-mass galaxies (e.g., Moskowitz & Walker 2020; Carlsten et al. 2021) and, if their presence remains in the critical HUG mass range (provided they meet the requirements of EIM), it could indicate the need to go beyond the standard CDM model.

Here we analyze the stellar count distribution of six ultrafaint dwarf (UFD) satellites of the Milky Way (MW) and the Large Magellanic Cloud (LMC) from Richstein et al. (2024). Their stellar masses are in the interesting HUG regime, 10^3–$10^4 \, M_\odot$, and they present stellar surface density profiles with cores. Here we consider whether these facts represent evidence for the DM deviating from the CDM paradigm. The work is presented as follows: Section 2 summarizes the observations and shows that the same radial profile reproduces all galaxies simultaneously within the error set by star counting. Section 3 outlines the

EIM-based procedure used to infer the DF needed to explain the observed profile with an assumed a potential. In Section 4, the procedure is applied to conclude that NFW potentials require unphysical negative DF and provide fits significantly worse than potentials with cores (Schuster–Plummer and ρ_{230} potentials). The conclusion that the satellites do not reside in NFW potentials depends on several simplifications and assumptions: steady state, stacking of profiles, spherical symmetry, shape of the potential, isotropic velocities, and unimportance of tidal forces and stellar feedback effects. All of them are discussed in Section 5, and the most compelling explanation for the existence of stellar cores in these dwarf galaxies remains a deviation from the CDM paradigm.

2. Data

Richstein et al. (2024) studied 10 UFD satellites of the MW and the LMC. Deep Hubble Space Telescope two-band photometry (F606W and F814W) allows them to select stars individually and to separate them from foreground and background contaminants. Only six of the UFDs have a field-of-view large enough to have good determination of structural parameters, and these are the targets employed in the present study: Horologium I, Horologium II, Hydra II, Phoenix II, Sagittarius II, and Triangulum II. The observed stellar counts of each galaxy were modeled using 2D Schuster–Plummer functions and exponentials, leaving free parameters that include the center, the characteristic radius, the ellipticity, and the orientation. These 2D fits were later used to construct 1D radial profiles as the number density of counts in ellipses with the ellipticity, orientation, and center of the best-fitting 2D functions. We use these 1D profiles in our work, both from the Schuster–Plummer function and the exponential since their differences quantify the systematic errors induced by the determination of centers, ellipticities, and orientations. The error in each radial bin is estimated as the Poisson noise arising from star counts.

From the above fits and ancillary data, Richstein et al. (2024) show the UFDs to have axial ratios from 0.55 to 1, $M_\star$ from 6×10^2 to $2.4 \times 10^4\,M_\odot$, and dynamical masses at the half-light radius between 10^5 and $5 \times 10^6\,M_\odot$. Thus, the ratio of dynamical mass to stellar mass within the half-light radius goes from 300 to 3000, with the exception of Sagittarius II where it is only around 10. It has been argued that Sagittarius II may be a globular cluster (GC) of large size (Longeard et al. 2021) but from the point of view of its surface density profile, it behaves as the rest. It is analyzed together with the others and separately, as discussed in Section 5. For further details on the data set and reduction, we refer to Richstein et al. (2024).

Figure 1 shows the 1D stellar surface density of the six UFDs normalized in x (size) and y (central density) using a least-squares procedure to set the scales so that the resulting profile, assumed to be a polynomial, is the same for all.[4] The reduced χ^2/ν of the fit,[5] 1.06, implies that all galaxies are well reproduced with a single profile with the scatter almost exclusively set by the star counting. This result is remarkable and implies that the profile in Figure 1 represents galaxies with

any ellipticity including completely round ones as expected in spherically symmetric systems in steady state. Moreover, this common profile has a central plateau or core whose logarithmic slope when $R \to 0$ is

$$\omega \equiv \frac{d \log \Sigma(R)}{d \log R} \simeq -0.026 \pm 0.058, \qquad (1)$$

determined from a linear fit to the 12 innermost points, chosen because they delineate the plateau (the black dashed line in Figure 1). The normalized data points in Figure 1 are the observations analyzed in this work. It represents stellar counts but we use them as proxies for the stellar mass density distribution, which is a good approximation for the UFDs having old stellar populations (e.g., Sacchi et al. 2021).

3. Eddington Inversion Method Approach

The details and tests of the technique are given elsewhere (J. Sánchez Almeida et al. 2024, in preparation), but here we summarize the approach used to compute the DF in the phase-space f required for the observed profile (Figure 1) to reside in a particular potential. For a spherically symmetric system of identical stars with isotropic velocity distribution, $f(\epsilon)$ depends only on the particle energy ϵ. (The impact of relaxing these assumptions is addressed in Section 5.) Then, the stellar volume density $\rho(r)$ turns out to be (e.g., Binney & Tremaine 2008, Section 4.3)

$$\rho(r) = 4\pi\sqrt{2} \int_0^{\Psi(r)} f(\epsilon)\sqrt{\Psi(r) - \epsilon}\,d\epsilon, \qquad (2)$$

with $\epsilon = \Psi - \frac{1}{2}v^2$ the relative energy per unit mass of a star and $\Psi(r) = \Phi_0 - \Phi(r)$ its relative potential energy. The symbol $\Phi(r)$ stands for the gravitational potential energy and Φ_0 is $\Phi(r)$ evaluated at the edge of the system. The previous equation can be rewritten as

$$\rho(r) = \int_0^{\epsilon_{\max}} f(\epsilon)\xi(\epsilon, r)d\epsilon, \qquad (3)$$

with

$$\xi(\epsilon, r) = 4\pi\sqrt{2\epsilon_{\max}}\sqrt{\left[\frac{\Psi(r)}{\Psi(0)} - \frac{\epsilon}{\epsilon_{\max}}\right]}\,\Pi(X - r), \qquad (4)$$

$\epsilon_{\max} = \Psi(0)$, X the radius implicitly defined as $\Psi(X)/\Psi(0) = \epsilon/\epsilon_{\max}$, and $\Pi(x)$ the step function,

$$\Pi(x) = \begin{cases} 0 & x \leqslant 0, \\ 1 & x > 0. \end{cases} \qquad (5)$$

The symbol $\xi(\epsilon, r)$ represents a family of densities that are characteristic of the potential and dependent on the energy ϵ. Then, according to Equation (3), the stellar density is just the superposition of these characteristic densities with the DF $f(\epsilon)$ giving the contribution of each energy to $\rho(r)$. (The characteristic densities for a Schuster–Plummer potential are shown as an example in the Appendix.) Following Equation (3), $f(\epsilon_i)$ could be retrieved by fitting the observable $\rho(r)$ with a linear superposition of $\xi(\epsilon_i, r)$ at various ϵ_i. (We will see below that ρ can be replaced with the projected stellar surface density, which is the true observable.) In practice, however, there is no error-proof way to discretize Equation (3). We approach the practical problem by expanding $f(\epsilon)$ as a

---

[4] $\log[\Sigma(R)/\Sigma(0)] = \sum_{i=0}^5 c_i[\log(R/b)]^i$, with $c_0, ..., c_5 = 0.262, -0.907, 1.019, 0.640, -1.619, -1.072$, valid for $0.07 \leqslant R/b \leqslant 2.7$ The symbols b and $\Sigma(0)$ stand for the scales in x and y, respectively. The half-mass–radius is 0.52b whereas the core radius, defined as in Equation (11), is 0.60b.

[5] χ^2 is the sum of the error normalized squares of the residuals whereas ν represents the degrees of freedom.
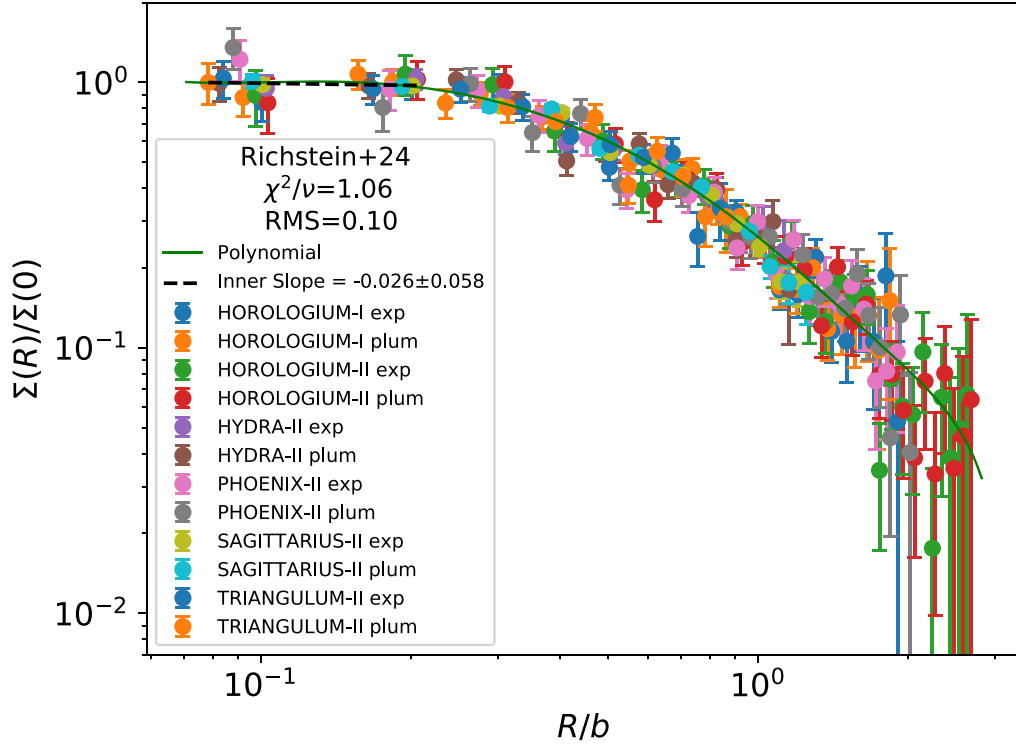
Figure 1. Stellar surface density profiles for six UFDs from Richstein et al. (2024), pieced together by rescaling in x and y using a least-square fit that gives the scales and assumes the same polynomial shape for all galaxies. The symbols represent different galaxies and reductions, as labeled, whereas the solid line shows the best-fitting polynomial. The dashed line corresponds to a linear fit to the innermost points of the profile. The best-fitting polynomial is close to a simple $y = 1/(1 + x^2)$ law (not shown). χ^2/ν stands for the reduced χ^2 of the fit with rms representing its root mean square.

polynomial of order n,

$$f(\epsilon) \simeq \epsilon_{\max}^{-3/2} \sum_{i=3}^{n} a_i (\epsilon/\epsilon_{\max})^i \,, \qquad (6)$$

so that

$$\rho(r) \simeq \sum_{i=3}^{n} a_i \, F_i(r), \qquad (7)$$

$$F_i(r) = \epsilon_{\max}^{-1/2} \int_0^1 \alpha^i \, \xi(\alpha \, \epsilon_{\max}, r) d\alpha, \qquad (8)$$

with $\alpha = \epsilon/\epsilon_{\max}$. Equation (7) gives a simple expansion of the stellar density $\rho(r)$ in terms of potential-dependent but known functions $F_i(r)$. The chosen functional form in Equation (6) is both flexible and, by starting at $i = 3$, it describes a system of finite mass despite the mass given by $\xi(\epsilon, r)$ diverges as $\epsilon^{-\gamma}$ when $\epsilon \to 0$, with $2 < \gamma < 3$ depending on the potential (J. Sánchez Almeida et al. 2024, in preparation). The normalization in Equation (6) has been chosen so that $F_i(r)$ does not depend on $\epsilon_{\max}$. The discretization in Equation (7) also holds for the projection of the volume density in the plane of the sky, i.e.,

$$\Sigma(R) \simeq \sum_{i=3}^{n} a_i \, S_i(R), \qquad (9)$$

$$S_i(R) = \int_0^1 \alpha^i \, \frac{\xi_\Sigma(\alpha \epsilon_{\max}, R)}{\sqrt{\epsilon_{\max}}} \, d\alpha, \qquad (10)$$

where $\Sigma(R)$ and $\xi_\Sigma(\epsilon_i, R)$ stand the 2D projection (i.e., the Abel transform) of $\rho(r)$ and $\xi(\epsilon_i, r)$, respectively. R represents the

radial coordinate in the plane of the sky projection, as in Section 2.

3.1. Actual Algorithm to Infer f(ε) from Σ(R)

Except for an arbitrary scaling parameterized by $\epsilon_{\max}$, Equations (6) and (9) provide a method to infer the DF $f(\epsilon)$ needed for a galaxy of observed mass surface density $\Sigma(R)$ to live in a given gravitational potential. A fitting algorithm using Equation (9) provides the coefficients a_i determining $f(\epsilon)$ through Equation (6). The characteristic densities in Equation (10) have to be computed numerically starting from the potential in a chain requiring at least two integrations: the Abel transform that projects the volume densities on the plane of the sky and the integral over all energies expressed by Equation (10). We compute the Abel transform using the direct method implemented in the `PyAbel` `Python` package (Hickstein et al. 2019). Then, the second integration is carried out using the `Simpson`'s rule from `Scipy` (Virtanen et al. 2020). The free parameters retrieved from fitting $\Sigma(R)$ are the amplitudes a_i together with the global radial scaling factor setting the width of the potential $r_{\rm sp}$ (see the Appendix), the latter making the fit nonlinear. The fits were carried out using a Bayesian approach. After the initialization using an unconstrained least-squares routine (`least_squares` from `scipy`; Virtanen et al. 2020), the posterior is explored using the ensemble sampler for Markov Chain Monte Carlo (MCMC) `emcee` (Foreman-Mackey et al. 2013). Several trial and error tests led us to set the order of the polynomial to 10, a value that provides enough flexibility to reproduce the inner plateau of the observed $\Sigma(R)$ (Figure 1). The priors in the Bayesian analysis are uninformative for $r_{\rm sp}$ and a_i ($0 < r_{\rm sp}/b \leqslant 10^3$ and $10^{-2} < |a_i| < 10^2$ relative to the values from the least-squares best fit). We also ask the outermost slope of the fitted $\log \Sigma(R)$ to be less
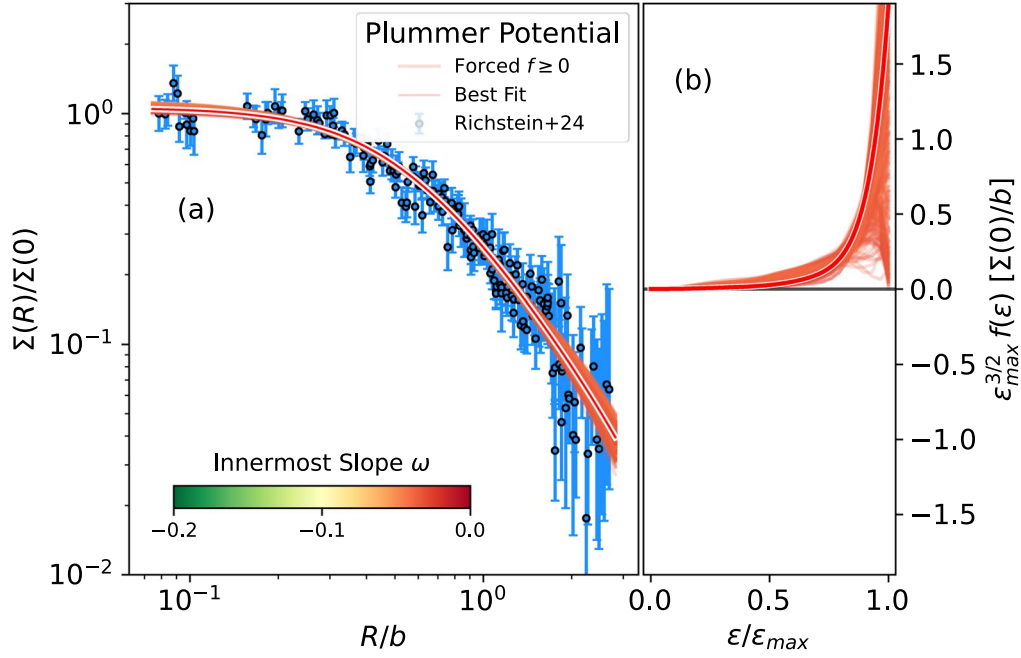
Figure 2. (a) Fits to the data in Figure 1 using $f(\epsilon)$ as free parameter and assuming the galaxies to reside in a Schuster–Plummer gravitational potential. The best fit is shown as a solid red line. The fits forced to have $f \geqslant 0$ are shown as colored solid lines, where the color code represents the innermost slope ($d \log \Sigma / d \log R$ when $R \to 0$) as indicated in the color bar. (b) $f(\epsilon)$ corresponding to the fits in (a) and using the same color code. Note that the best unconstrained fit yields $f \geqslant 0$ everywhere.
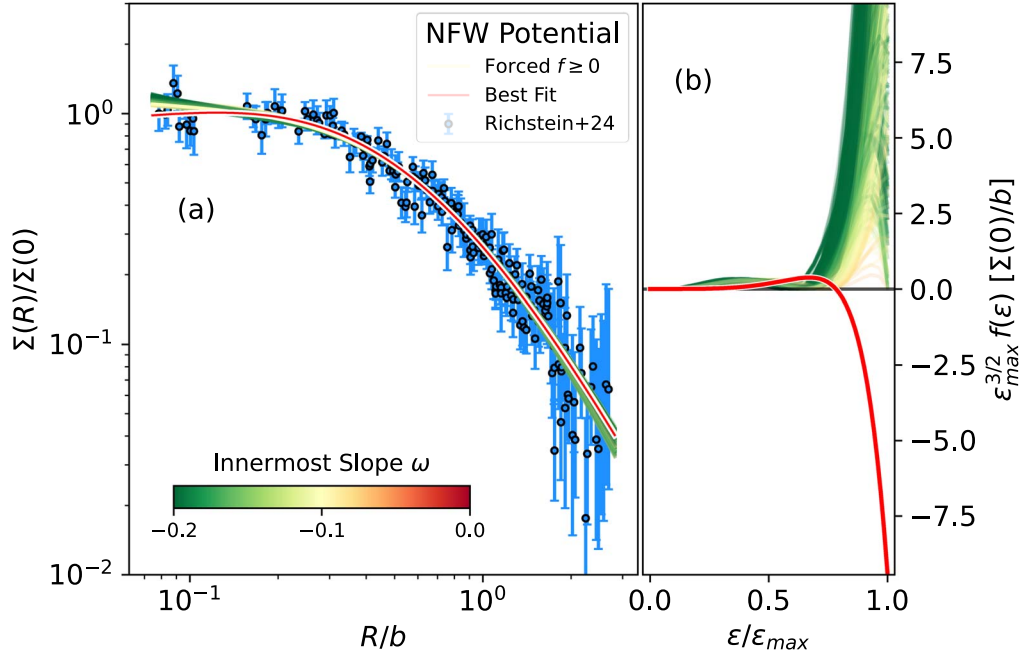

Figure 3. Same as Figure 2 but assuming the galaxies to reside in a NFW potential. The color code is the same as that employed in Figure 2. Note that the best fit requires an unphysical $f < 0$ (the red solid line in panel (b)) and that the fits forced to have $f \geqslant 0$, contrarily to the observation, present quite negative inner slopes ω (the coloring is green–yellow rather than orange–red).

than -2, thus preventing $\Sigma(R)$ from having infinite mass outside the observed radii. In addition, we force $f \geqslant 0$ so that potential and observation are physically consistent. All in all, the fits have nine free parameters (eight a_i plus $r_{\rm sp}$), which is much smaller than the 207 observed points in Figure 1. The posterior was explored with 32 walkers and 6000 samples—none of the results reported below depend on these exact values.

The algorithm passed a number of sanity checks with systems where the DM distribution is known, namely, GCs and simulated dwarf galaxies. In addition, back-of-the-envelope

estimates assure the stars in UDFs to be collisionless, as required by EIM.

4. Results

The DF fitting algorithm in Section 3 was applied to the stellar surface density data of Richstein et al. (2024) rescaled as in Figure 1. Thus, we consider the observed profile to represent a spherically symmetric galaxy and assume its velocities to be isotropic, assumptions critically inspected in Section 5. The
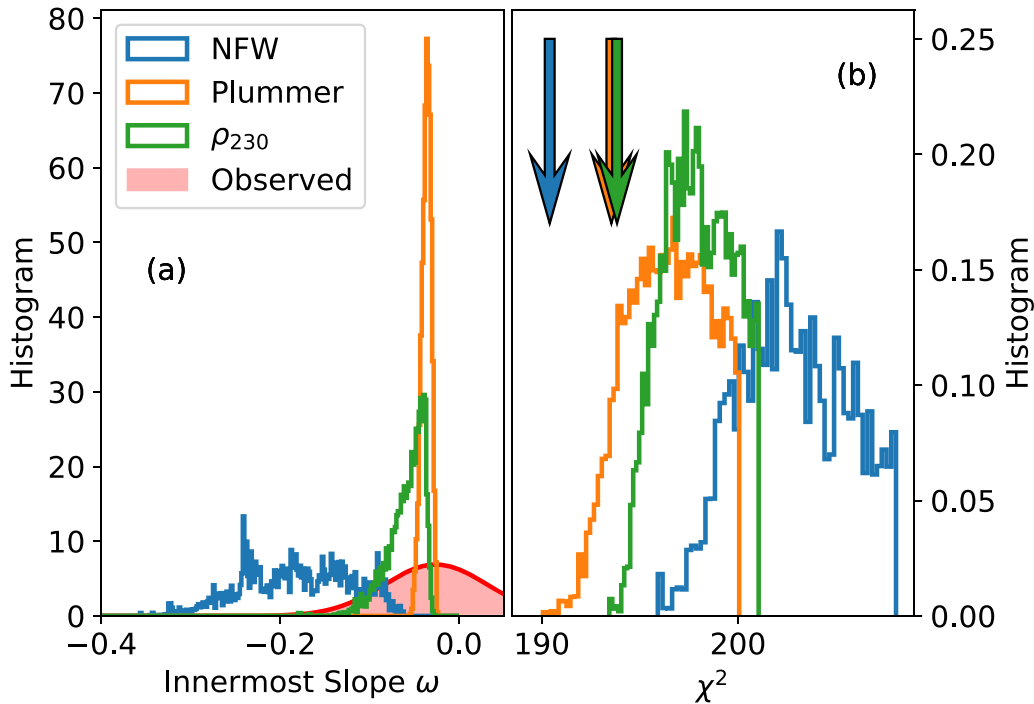
Figure 4. Summary plot used to estimate confidence limits. (a) Histograms with the innermost slopes for the fits with the three gravitational potentials explored in the work (see the inset). The red histogram represents the observed value (Equation (1)). (b) Distribution of χ^2 of the fits for the three potentials when forcing $f \geqslant 0$. The arrows represent the χ^2 of the best fit obtained with unconstrained $f(\epsilon)$. The color code is the same in (a) and (b).

results considering a Schuster–Plummer potential (core) and an NFW potential (cusp) are shown in Figures 2 and 3, respectively. There are two clear differences between them: (1) the best-fitting NFW potential needs and unphysical $f < 0$ (Figure 3(b), the red solid line) which is not required in the case of a Schuster–Plummer potential (Figure 2(b)); (2) the innermost slope obtained when the fits are forced to have physically sensible $f \geqslant 0$ are distinctly negative for the NFW potential and near zero for the Schuster–Plummer potential (compare the coloring of the thin lines in Figures 2 and 3).

Two other more subtle differences are brought out in Figure 4: (3) the $f \geqslant 0$ Schuster–Plummer potential fits are significantly better than the corresponding NFW potential fits (see their χ^2 in Figure 4(b)); and (4) the distribution of innermost slopes of the NFW potential fits are in tension with the observed innermost slope (Equation (1)); see the red and the blue histograms in Figure 4(a). This tension goes away in the case of a Schuster–Plummer potential (the orange histogram in Figure 4(a)). We also analyze the observed stellar surface density assuming the gravitational potential stemming from a density profile $\rho_{230} \propto 1/(1 + r^2)^{3/2}$, which is similar to Schuster–Plummer in the center and to NFW in the outskirts (see the pink dashed line in Figure 5). It is also consistent with the observations, very much like the Schuster–Plummer potential (Figure 4).

The distributions in Figure 4 are used to work out confidence levels discarding the observed UFDs to reside in NFW potential under the assumption of spherical symmetry and velocity isotropy. The χ^2 of the best fitting function is 4.5σ off the mean of the χ^2 corresponding to the $f \geqslant 0$ NFW potential fits (see blue arrow and histogram in Figure 4(b)). (Here and throughout, σ represents the standard deviation of the named distribution.) The best NFW fit has been constructed to have the lowest χ^2, but only in the case of the NFW potential does

the best fit not overlap with the distribution of χ^2 for $f \geqslant 0$ (Figure 4(b)). Assuming that a 2σ decrease of the best-fit χ^2 would still be consistent with the $f \geqslant 0$ χ^2 distribution, we can set the confidence level as follows. Since the NFW best-fit χ^2 is 4.5σ off, it would require an extra 2.5σ fluctuation. Being conservative and assuming a Gaussian tail for the χ^2 distribution, a 2.5σ fluctuation has a probability of 0.6%; therefore, we can discard the observed UFDs to reside in an NFW potential with a 99.4% confidence. The same argumentation applied to the Schuster–Plummer and the ρ_{230} potentials yields full consistency of the best fits with $f \geqslant 0$ fits. A similar exercise can be carried out with the distribution of innermost slopes ω represented in Figure 4(a). The $f \geqslant 0$ NFW potential fits yield a distribution with a mean and standard deviation of -0.18 ± 0.06; therefore, its mean is 2.7σ away from the observed value (Equation (1)). It is off by only 0.18σ and 0.58σ in the case of Schuster–Plummer and ρ_{230}, respectively (Figure 4(a)). Assuming a Gaussian tail for the distribution of errors, the probability for fluctuation $>2.7\sigma$ is 0.004, which would discard the existence of an NFW potential with 99.6% confidence. A more conservative approach of setting a confidence level is computing the probability that the innermost slopes are consistent with the observed slope within 1σ, i.e., $\omega \geqslant -0.084$. It is only 3% for the NFW potential whereas it is 100% for the Schuster–Plummer potential and 87% for the ρ_{230} potential. The 3% value discards the observed galaxies to reside in an NFW potential with 97% confidence.

Figure 5 shows the correspondence between the stellar surface density profile and the mass surface densities producing the best-fitting potentials. The global scaling factor remains unconstrained in our procedure (Section 3.1) and has been set so that the mass giving rise to the potential is 500 times $M_\star$ (representative of the observations; see Section 2). Interestingly, the core radius R_c of the stars and the potentials are very
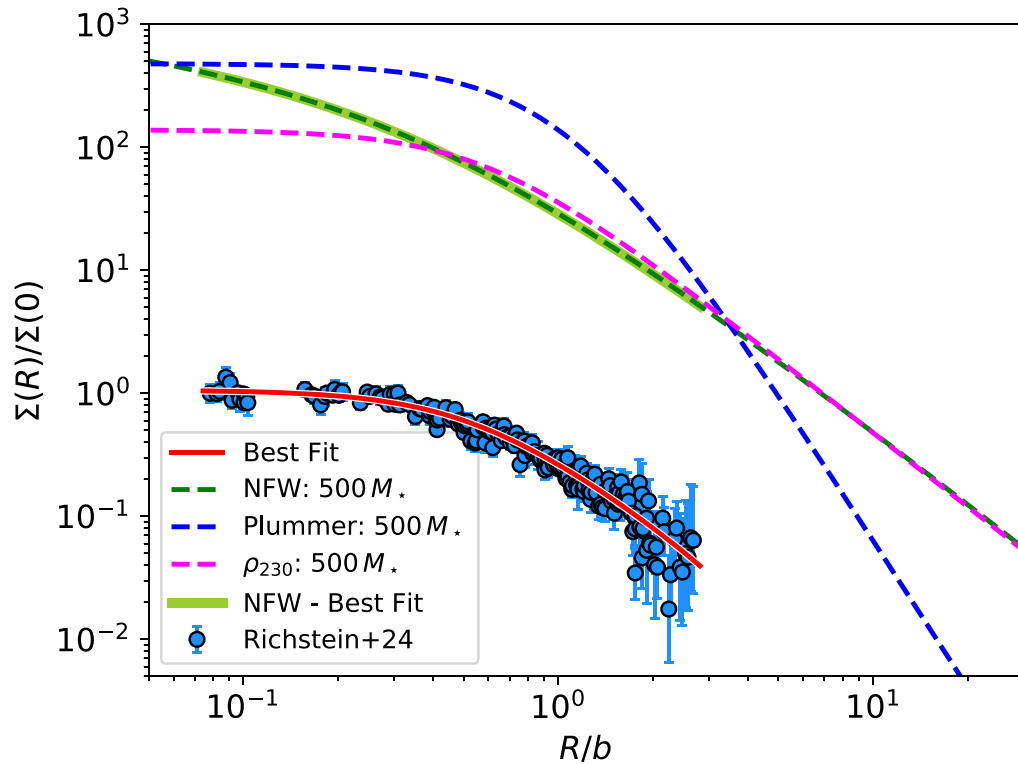
Figure 5. Observed stellar surface density (the symbols) and its best fit assuming a Schuster–Plummer potential (the red solid line). The plot shows the mass surface density that gives rise to the best fitting Schuster–Plummer potential (the blue dashed line), the NFW potential (the green dashed line), and the ρ_{230} potential (the magenta dashed line). The vertical scaling was chosen to be representative of the UFDs, so that the mass creating the potential is 500 times the observed stellar mass. The contribution from the stars to the overall potential has been subtracted out in the solid yellow–green line. The result is virtually indistinguishable from the original profile (the green dashed line), showing the self-gravity of the stars to be negligible.

similar. Defining as core radius when the surface density is half the maximum value, $\Sigma(R_c) = \Sigma(0)/2$,

$$\log[R_c^{\text{Potential}}/R_c^{\star}] = \begin{cases} 0.06 \pm 0.08 & \text{Plummer,} \\ -0.01 \pm 0.13 & \rho_{230}, \end{cases} \quad (11)$$

where $R_c^{\star}$ and $R_c^{\text{Potential}}$ stand for the core radius of the stars and the potential, respectively. The error bars come from the scatter of the MCMC sampling of the posterior.

5. Discussion and Conclusions

The main finding of this study is that six small UFD galaxies do not reside in NFW potentials, a conclusion supported with a confidence level $\geqslant 97\%$ (Section 4). The stellar mass of these systems is as low as 10^3–$10^4\,M_{\odot}$, for which baryon feedback should be unable to modify the shape of the CDM potential (Section 1), usually represented by an NFW potential. Simultaneously, the observed UFDs are consistent with potentials with an inner core as predicted by many alternatives to CDM. Taken at face value, this result points to the DM deviating from collisionless CDM. However, open to scrutiny, the used analysis hinges on several assumptions that could blur such seemingly clear-cut evidence. Below we examine the assumptions to conclude that a deviation from the CDM paradigm still seems to be the main interpretation of the observed stellar cores.

(1) The main observational constraint disfavoring NFW potentials is the innermost slope of $\Sigma(R)$, ω, being $\simeq 0$ (Equation (1)). The constraint is fairly robust largely independent of the method to compute azimuthal average profiles (Section 2). The stacking to produce the reference observed profile (Figure 1) does not influence it either. We tried several alternatives, and they all render cored stellar surface density profiles, which, subject to our analysis, are incompatible with NFW potentials.

(2) The EIM adopted in the work assumes the velocities to be isotropic (Equation (2)). However restrictive, this assumption does not seem to produce the tension between stellar cores and NFW potentials because the tension remains even when the assumption is dropped. The theorem posed by An & Evans (2006) relates the innermost slope of stars with the velocity anisotropy parameter, discarding all radially biased velocity distributions provided $\omega \simeq 0$. The Osipkov–Merrit model describes a case in between isotropic and radial, with isotropic orbits at the center that progressively become radial in the outskirts, and it is inconsistent with NFW potentials too (Sánchez Almeida et al. 2023). Circular orbits offer a chance to reconcile NFW potentials with stellar cores (e.g., Sánchez Almeida et al. 2023); however, they are expected to be uncommon among the smallest galaxies. Both the hierarchical growth of galaxies by accretion and the outflows driven by central starbursts cause radial rather than tangential motions. This is indeed found in cosmological numerical simulations of dwarf galaxy formation, which produce Osipkov–Merrit-like velocity anisotropy (e.g., El-Badry et al. 2017; Orkney et al. 2023) or quasi-isotropic orbits (Gonzalez-Samaniego et al. 2017). This trend is also found in dwarf spheroidal galaxies with observed kinematics (e.g., Massari et al. 2020; Kowalczyk & Łokas 2022). More complex anisotropies still need to be fully discarded (e.g., Strigari et al. 2017).

(3) The fact that the analyzed galaxies are satellites rather than centrals may have changed the shape of their DM potential

through tidal forces with the central galaxy and other satellites. Two arguments seem to minimize the influence of these interactions. First, elaborate CDM-only cosmological numerical simulations show that the DM haloes maintain their identity and the same shape along 30 orders of magnitude in mass (van den Bosch et al. 2018; Wang et al. 2020). Since small haloes are satellites, this simulation shows that the tidal forces arising from the main source of gravitation (i.e., from DM) do not change the shape to be expected in CDM satellite haloes. Second, the history of tidal disruptions suffered by different satellites is different so that different satellites should present different profiles if the shape were set by the tidal influence, and this is not the case with the stellar distribution in UFDs (Figure 1).

(4) Spherical symmetry of both DM and stars is assumed in the EIM analysis. In principle, this is not consistent with the fact that the observed axial ratio of the UFDs often differs from 1 (Section 2). However, we note that all observed stellar density profiles collapse to the same profile within errors (Figure 1). Since this profile is independent of that axial ratio, it is the one to be expected from a purely spherical stellar system, for which EIM applies consistently. Moreover, one of the targets (Sagittarius II) is round within errors (Richstein et al. 2024). We analyze it individually with a result consistent with the whole set: NFW potential fits are significantly worse than Schuster–Plummer and the required innermost slope ω differs from zero when forcing $f \geqslant 0$. In addition, Sánchez Almeida et al. (2024) show how the incompatibility between NFW potentials and stellar cores also remains for axisymmetric systems suggesting that it is more fundamental than, and not attached to, the spherical symmetry assumption. The idea that the incompatibility is not due to the spherical symmetry assumption is also advanced in An & Evans (2009).

(5) As soon as they possess cores, the actual details of the potential are not important to grant agreement with stellar cores. This conclusion is attested by the agreement of the observations with both Schuster–Plummer and ρ_{230} potentials (Figures 4 and 5) and also by the battery of tests carried out for other potentials by Sánchez Almeida et al. (2023). The use of NFW to represent CDM also seems to be unessential since the Einasto profiles, which are also a good representation of the CDM halos, are also incompatible with stellar cores (Sanchez Almeida 2024). The Einasto profiles do not diverge at the center indicating that the incompatibility is not artificially set by the mathematical singularity of the NFW profiles when $r \to 0$.

(6) The hypothesis that stellar feedback is unable to modify the gravitational potential of the observed UFDs is backed up by cosmological numerical simulations (Section 1); therefore, it depends on the assumed subgrid physics for the feedback. Increasing the effectiveness of the feedback may reduce the stellar mass threshold able to influence, but not much. The order of magnitude estimate by Peñarrubia et al. (2012, Figure 2 of their paper) shows that the threshold is set by energy conservation—there is not enough energy in supernovas to turn NFW potentials into core potentials when $M_\star \ll 10^6 M_\odot$. The UFDs that we analyze are more than 2 orders of magnitude less massive than this limit and so the ineffectiveness of stellar feedback seems to be granted.

(7) The self-gravity of the stars is not considered in our analysis, implicitly assuming the stellar mass to be negligible compared to the DM mass. This is a good approximation for most UFDs (Section 2), and since the observed surface densities are the same for all (Figure 1), this assumption seems to be safe.

(8) The fact that Sagittarius II may be an extended GC (Section 2) is not relevant to the analysis. The whole procedure was repeated withdrawing Sagittarius II without any difference that could modify the above conclusions.

To sum up, this work shows that six UFD galaxies reside in cored gravitational potentials. Since stellar feedback should be inoperative in their stellar mass regime (HUG), the best explanation seems to be that the DM deviates from the nature assumed in the standard ΛCDM cosmological model. The standard model provides an extremely good approximation to reality but is likely not the last theory (Peebles 2021). Studying the kind of galaxies analyzed here may provide a gateway to go beyond.

Appendix
Characteristic Densities in the Case of a Schuster–Plummer Potential

Consider the gravitational potential generated by a mass distribution following a Schuster–Plummer density profile, i.e.,

$$\rho_{SP}(r) = \frac{\rho_{sp}}{[1 + (r/r_{sp})^2]^{5/2}}, \qquad (A1)$$

where ρ_{sp} and r_{sp} are the central density and the characteristic radial scale, respectively. The gravitational potential produced by this cored density profile is (e.g., Sánchez Almeida et al. 2023,

Equation (A14))

$$\Psi_{SP}(r) = \frac{\epsilon_{max}}{[1 + (r/r_{sp})^2]^{1/2}}, \tag{A2}$$

with $\epsilon_{max} = 4\pi G \rho_{sp} r_{sp}^2 / 3$. Equation (4) renders,

$$\xi(\epsilon, r) = \sqrt{\epsilon_{max}} \, h(\epsilon/\epsilon_{max}, r/r_{sp}), \tag{A3}$$

$$h(\alpha, \beta) = 4\pi\sqrt{2} \, \sqrt{[(1 + \beta^2)^{-1/2} - \alpha]} \, \Pi(\beta - \beta_X), \tag{A4}$$

with $\beta_X = \sqrt{1 - \alpha^2}/\alpha$.

ORCID iDs

Jorge Sánchez Almeida ⓘ https://orcid.org/0000-0003-1123-6003
Ignacio Trujillo ⓘ https://orcid.org/0000-0001-8647-2874
Angel R. Plastino ⓘ https://orcid.org/0000-0001-5848-0770

References

An, J. H., & Evans, N. W. 2006, ApJ, 642, 752
An, J. H., & Evans, N. W. 2009, ApJ, 701, 1500
Bechtol, K., Birrer, S., Cyr-Racine, F.-Y., et al. 2022, arXiv:2203.07354
Binney, J., & Tremaine, S. 2008, Galactic Dynamics: Second Edition (Princeton, NJ: Princeton Univ. Press)
Carlsten, S. G., Greene, J. E., Greco, J. P., Beaton, R. L., & Kado-Fong, E. 2021, ApJ, 922, 267
Chan, T. K., Keres, D., Onorbe, J., et al. 2015, MNRAS, 454, 2981
Ciotti, L. 2021, Introduction to Stellar Dynamics (Cambridge: Cambridge Univ. Press)
Di Cintio, A., Brook, C. B., Macciò, A. V., et al. 2014, MNRAS, 437, 415
El-Badry, K., Wetzel, A. R., Geha, M., et al. 2017, ApJ, 835, 193
Foreman-Mackey, D., Hogg, D. W., Lang, D., & Goodman, J. 2013, PASP, 125, 306
Gonzalez-Samaniego, A., Bullock, J. S., Boylan-Kolchin, M., et al. 2017, MNRAS, 472, 4786
Governato, F., Brook, C., Mayer, L., et al. 2010, Natur, 463, 203
Hayashi, K., Chiba, M., & Ishiyama, T. 2020, ApJ, 904, 45
Hickstein, D. D., Gibson, S. T., Yurchak, R., Das, D. D., & Ryazanov, M. 2019, RScI, 90, 065115
Jackson, R. A., Martin, G., Kaviraj, S., et al. 2021, MNRAS, 502, 4262
Kowalczyk, K., & Łokas, E. L. 2022, A&A, 659, A119
Longeard, N., Martin, N., Ibata, R. A., et al. 2021, MNRAS, 503, 2754
Massari, D., Helmi, A., Mucciarelli, A., et al. 2020, A&A, 633, A36
Moskowitz, A. G., & Walker, M. G. 2020, ApJ, 892, 27
Navarro, J. F., Frenk, C. S., & White, S. D. M. 1997, ApJ, 490, 493
Oh, S.-H., Hunter, D. A., Brinks, E., et al. 2015, AJ, 149, 180
Orkney, M. D. A., Taylor, E., Read, J. I., et al. 2023, MNRAS, 525, 3516
Peñarrubia, J., Pontzen, A., Walker, M. G., & Koposov, S. E. 2012, ApJL, 759, L42
Peebles, P. J. E. 2021, arXiv:2106.02672
Read, J. I., Agertz, O., & Collins, M. L. M. 2016, MNRAS, 459, 2573
Richstein, H., Kallivayalil, N., Simon, J. D., et al. 2024, ApJ, 967, 72
Sacchi, E., Richstein, H., Kallivayalil, N., et al. 2021, ApJL, 920, L19
Sanchez Almeida, J. 2024, RNAAS, 8, 167
Sánchez Almeida, J., Plastino, A. R., & Trujillo, I. 2023, ApJ, 954, 153
Sánchez Almeida, J., Plastino, A. R., & Trujillo, I. 2024, A&A, in press, arXiv:2407.16519
Strigari, L. E., Frenk, C. S., & White, S. D. M. 2017, ApJ, 838, 123
van den Bosch, F. C., Ogiya, G., Hahn, O., & Burkert, A. 2018, MNRAS, 474, 3043
Virtanen, P., Gommers, R., Oliphant, T. E., et al. 2020, NatMe, 17, 261
Wang, J., Bose, S., Frenk, C. S., et al. 2020, Natur, 585, 39